Supplementary Information (SI) for Materials Chemistry Frontiers.
This journal is © the Partner Organisations 2026

Electronic Supplementary Information

Ni–OH Promoted Water Dissociation on Pt/Ni Dual Active Sites for Accelerated Alkaline Hydrogen Evolution

Shubing Li,[‡ 1] Tianyu Xia,[‡ 1] * Yuxin Zhao,[1] Lingrui Wang,[1] Fan Meng,[2] * Noriyoshi Arai,[2] Haizhong Guo[1,3] * and Rongming Wang [4] *

[1] School of Physics and Laboratory of Zhongyuan Light, Zhengzhou University, Zhengzhou 450001, China

[2] Department of Mechanical Engineering, Keio University, 3-14-1 Hiyoshi, Kohoku-ku, Yokohama, 2238522, Kanagawa, Japan

[3] Institute of Quantum Materials and Physics, Henan Academy of Sciences, Zhengzhou 450046, China

[4] Beijing Key Laboratory for Magneto-Photoelectrical Composite and Interface Science, State Key Laboratory for Advanced Metals and Materials, University of Science and Technology Beijing, Beijing 100083, China

‡ Shubing Li and Tianyu Xia contributed equally to this work.

*Address correspondence to Tianyu Xia, tyxia@zzu.edu.cn; Fan Meng, mengfan@keio.jp; Haizhong Guo, hguo@zzu.edu.cn; Rongming Wang, rmwang@ustb.edu.cn

1. Experimental

1.1 Chemicals and reagents

Platinum(II) acetylacetonate ($Pt(acac)_2$), nickel(II) acetylacetonate ($Ni(acac)_2$) are purchased from Thermo scientific. Cetyltrimethylammonium Chloride (CTAC, 97%), glucose (99.5%), oleylamine (> 98%) are purchased from Aladdin. Commercial Pt/C (40% Pt) is purchased from Macklin. N, N-Dimethylformamide (DMF, 99.5%) is purchased from Yongda Chemical. Ethanol anhydrous (99.7%) is purchased from Fuyu Chemical. All the above reagents are used as received without further purification. Deionized (DI) water used in the experiments is filtered by a Millipore Autopure system (18.2 MΩ·cm).

1.2 Synthesis of PtNi MBNs and PtNi NPs

0.05 mmol $Pt(acac)_2$, 0.1 mmol $Ni(acac)_2$, 0.33 mmol glucose, and 0.1 mmol CTAC were dissolved in 20 mL of oleylamine via ultrasonicating for 1.5 h. Then the mixed solution was transferred to a 25 mL reaction kettle and maintained 220 ℃ for 12 h. Then, the product was naturally cooled to room temperature, centrifugally collected and washed with ethanol to obtain PtNi MBNs. Under the same conditions, replacing oleylamine with DMF yields PtNi NPs.

1.3 Characterizations

Transmission electron microscopy (TEM), High-resolution TEM (HRTEM), High-angle annular dark-field scanning TEM (HAADF-STEM), and Energy dispersive spectroscopy (EDS) are recorded on an FEI Talos F200S electron microscope with an accelerating voltage of 200 kV. Scanning Electron Microscope (SEM) is recorded on Guoyi Quantum SEM5000X. X-ray diffraction (XRD) is performed on a SmartLab with Cu−Kα radiation (1.5406 Å). X-ray photoelectron spectroscopy (XPS) is conducted by the Thermo Scientific K-Alpha system, used Al Kα radiation (1486.6 eV) as the excitation source, and corrected with C 1s line at 284.8 eV. The types and contents of chemical elements in the samples are measured by Inductively coupled plasma mass spectrometry (ICP-MS) (Agilent 7800). *In situ* Raman spectroscopy is performed on Princeton Instruments with an excitation laser beam wavelength of 532 nm.

1.4 Electrochemical Measurements

All electrochemical measurements of HER are recorded on a CHI 760E electrochemical workstation with a standard three-electrode system at room temperature. The working electrode, counter electrode and reference electrode are Rotating Disk Electrode (diameter: 5 mm, area: 0.196 cm^2), graphite rod and KCl-saturated Ag/AgCl electrode, respectively. The working electrode is prepared by homogeneously mixing appropriate catalyst inks of PtNi MBNs, PtNi NPs, and commercial Pt/C (catalyst loading: 10 μg_{pt} cm^{-2}, respectively) with ethanol followed by adding 5 μL Nafion solution (5.0 wt%) to form a homogeneous ink, drop on the working electrode, and dry it naturally at room temperature. All electrochemical measurements were conducted in 1 M KOH solution.

Before electrochemical measurements in different electrolytes, the reference electrode was corrected through testing the reversible hydrogen electrode (RHE) potential, all potentials reported are converted to the standard reversible hydrogen electrode (RHE) according to the Nernst equation:

$$E_{vs\ RHE} = E_{vs\ Ag/AgCl} + 0.0592 \times pH + 0.197\ (pH = 14) \qquad (1)$$

Tafel slopes are determined by plotting the overpotential *vs.* the logarithm of current density (log |j|). EIS is conducted in the frequency range from 10^{-1} Hz to 10^5 Hz at a scan rate of 5 mV s^{-1} in various HER overpotentials. The resistance of the solution (R_s) resulting from the Nyquist plot is used to correct the ohmic drop (iR-correction) for the HER measurement. All polarization curves are corrected with 70% iR compensation. The corrected potential can be obtained by $E_{corrected} = E_{RHE} - iR_s$. Electrocatalytic durability tests are conducted by subjecting the ink catalyst loaded on carbon paper (with a loading of 51 μg cm^{-2}) to Chronopotentiometry (CP) measurements. Accelerated durability testing (ADT) is performed using cyclic voltammetry (CV) between 0 and 2 V (*vs*. RHE) at a scan rate of 100 mV s^{-1} for 10,000 cycles. CO stripping tests are conducted by first exposing the sample to a CO-saturated 1 M KOH solution for 30 minutes to allow CO adsorption, followed by performing CV measurements at a scan rate of 50 mV s^{-1} under continuous N_2 purging.

The mass activity is calculated based on the following equation: Mass Activity = $\frac{I}{m}$, where I (A) is the measured current, m (mg) is the mass of Pt loaded on the electrode. The turnover frequency (TOF) is calculated based on the following equation: $TOF = \frac{I}{2Fn}$, where I (A) is the measured current, F is the Faraday constant (96485 C mol^{-1}), $n = \frac{m}{M}$, n (mol) is the molar amount of Pt loaded on the electrode, m is the mass of Pt, and M is the molecule weight.

1.5 Molecular dynamics simulation

This study employed the Gromacs software package[1] to perform molecular dynamics simulations, investigating the configurational orientation characteristics of small molecules on the PtNi alloy (001) crystal surface in aqueous solution. The simulation system consisted of KOH solution and metal surface, with the TIP4P model selected for H_2O molecules. The General AMBER Force Field 2 (GAFF2) was used to describe the solution, [2] while the Lennard-Jones parameters from the UFF (Universal Force Field) were applied to Pt and Ni atoms on the metal surface. [3] The metal-molecule interactions were calculated using Lorentz-Berthelot combining rules. [4]

$$\sigma_{ij} = \frac{\sigma_i + \sigma_j}{2} \quad (2)$$

$$\epsilon_{ij} = \sqrt{\epsilon_i + \epsilon_j} \quad (3)$$

The simulation box dimensions were x, y = 13.55 nm and z = 9.45 nm, with an alloy layer thickness of z = 1.253 nm. The system contained 1000 KOH molecules and 50,000 TIP4P water molecules, corresponding to the experimental 1 M KOH electrolyte. The metal surface was modeled as a PtNi alloy with the Miller-indexed (001) crystallographic plane, with lattice parameters provided in Table S3. The top and bottom atomic layers of the simulation box consisted of Pt and Ni, respectively, to simultaneously investigate the influence of both metal surfaces on H_2O molecule orientation. The positions of metal atoms were fixed throughout the simulation to prevent lattice variations induced by thermal fluctuations.

After energy minimization and equilibration, production simulations were performed under the canonical (NVT) ensemble with a constant temperature of 298 K

and an integration time step of 1 fs. The V-rescale thermostat was employed for temperature control, and atomic charges were assigned using the Gasteiger method. [5] Long-range electrostatic interactions were treated with the Particle Mesh Ewald (PME) method, with a cutoff distance of 1.2 nm. Molecular trajectories were visualized and analyzed using OVITO software. [6]

2. Figures and tables

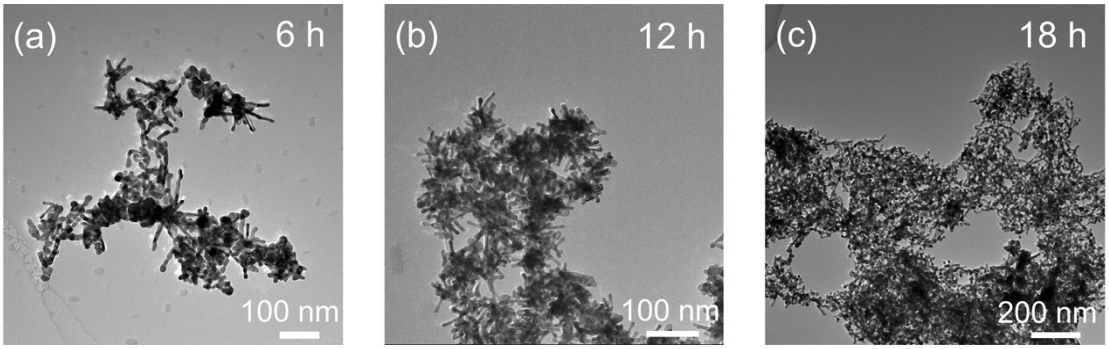

Fig. S1. TEM images of the multibranched structure formation process at (a) 6h, (b) 12h, and (c) 18h.

As shown in the transmission electron microscopy (TEM) images in **Fig. S1**, after a reaction time of 6 hours (Fig. S1a), the product already exhibits a clear trend of anisotropic growth, but the branches are uneven in length and the structure is incomplete. By 12 hours (Fig. S1b), uniform and well-defined multibranched nanostructures were fully formed. However, extending the reaction time to 18 hours resulted in structural coarsening (Fig. S1c), favoring the formation of more stable network structures.

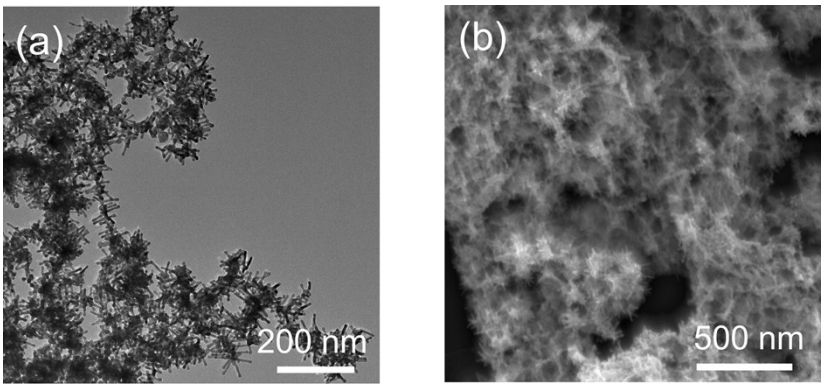

Fig. S2. (a) TEM and (b) SEM images of PtNi MBNs.

The morphology and structure of PtNi MBNs are revealed in the TEM image shown in Fig. S2a, while Scanning Electron Microscope (SEM) image in Fig. S2b clearly demonstrate PtNi MBNs excellent dispersion.

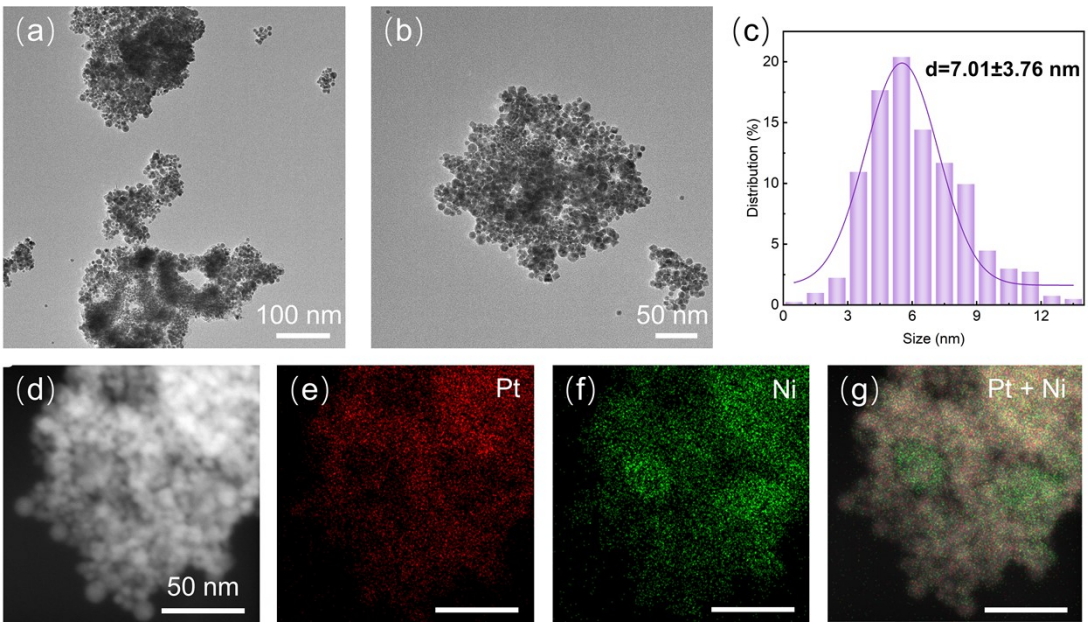

Fig. S3. (a-b) TEM images of PtNi NPs. (c) Particle size distribution of PtNi NPs. (d-g) HAADF-STEM images and the corresponding EDS elemental mapping images of PtNi NPs.

Fig. S3a and b reveals that the PtNi nanoparticles (PtNi NPs) exhibit smooth surfaces with particle sizes of approximately 4–6 nm (Fig. S3c). Such small dimensions promote aggregation of PtNi NPs. As evidenced by the HAADF-STEM images and elemental mapping in Fig. S3d-g, Pt and Ni elements are homogeneously distributed throughout PtNi NPs. This uniform distribution stands in stark contrast to the surface-enriched structure observed in the aforementioned PtNi MBNs.

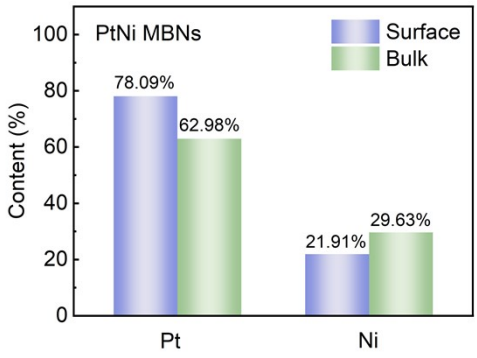

Fig. S4. Pt and Ni surface contents fitted by XPS compared with the bulk contents detected by ICP-MS.

The results demonstrate that PtNi MBNs exhibit a heterogeneous compositional distribution: Pt is uniformly distributed, while Ni is predominantly located in the interior. This finding aligns with our observations from the HAADF-STEM along with elemental mapping (Fig. 1f-i).

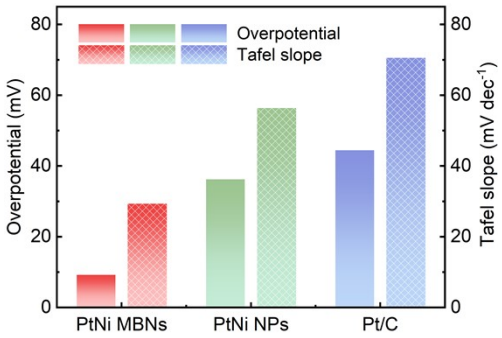

Fig. S5. Overpotentials and Tafel slopes at a current density of 10 mA cm^{-2}.

Fig. S5 presents a bar chart comparing the overpotential at 10 mA cm^{-2}, and the Tafel slopes for the three catalysts. It can be observed that the PtNi MBNs demonstrates the best overall performance, showing significant improvement over commercial Pt/C.

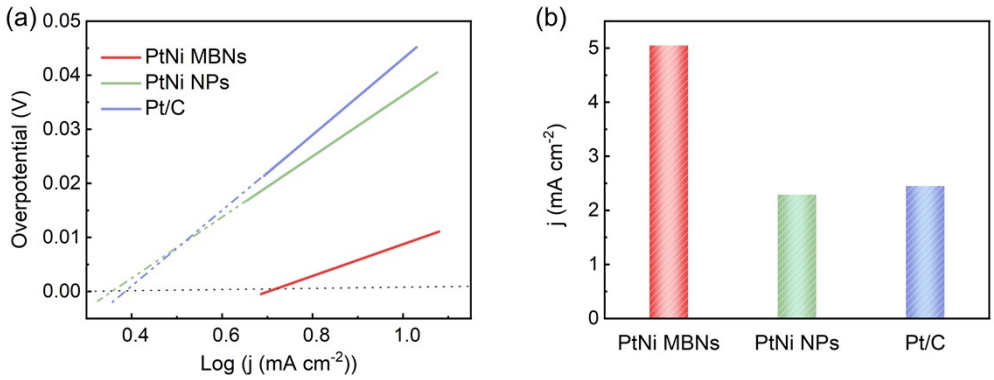

Fig. S6. (a) The j_0 of PtNi MBNs, PtNi NPs, and commercial Pt/C catalysts. (b) Bar chart of the j_0 at equilibrium ($\eta = 0$) for PtNi MBNs, PtNi NPs, and commercial Pt/C catalysts.

As another fundamental parameter for evaluating electrocatalytic reaction kinetics, the exchange current density (j_0) directly reflects both the intrinsic activity of the catalyst and the charge transfer efficiency at the electrode/electrolyte interface. Theoretical studies confirm that a higher j_0 value corresponds to a lower activation energy barrier and faster reaction kinetics. [7] As shown in Fig. S6, quantitative analysis reveals that PtNi MBNs possess an exceptional exchange current density (j_0) of 5.05 mA cm^{-2}, substantially higher than that of control catalysts. This result provides direct evidence for their superior intrinsic activity, charge transfer efficiency, and ultrafast reaction kinetics in the HER process.

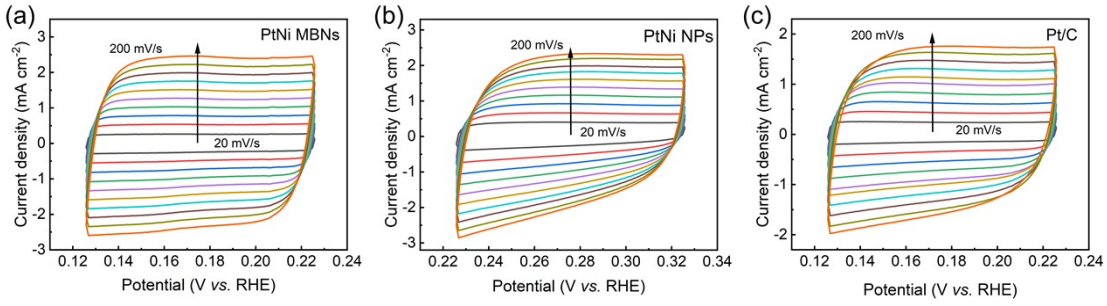

Fig. S7. CV curves of (a) PtNi MBNs, (b) PtNi NPs, and (c) commercial Pt/C at various rotation rates from 20 to 200 mV s^{-1} in 1 M KOH.

Double-layer capacitance (C_{dl}) was obtained based on the CV of the double-layer region (non-Faradaic reaction region). By plotting $\Delta j/2 = (j_{anodic} - j_{cathodic})/2$ against the scan rates (20, 40, 60, 80, 100, 120, 140, 160, 180 and 200 mV s^{-1}), the slope of the fitting line was regarded as the geometric C_{dl} of catalysts (Fig. S7). The j_{anodic} and $j_{cathodic}$ indicate the current density of the anodic and cathodic sweeps at the midpoint of the potential region, respectively.

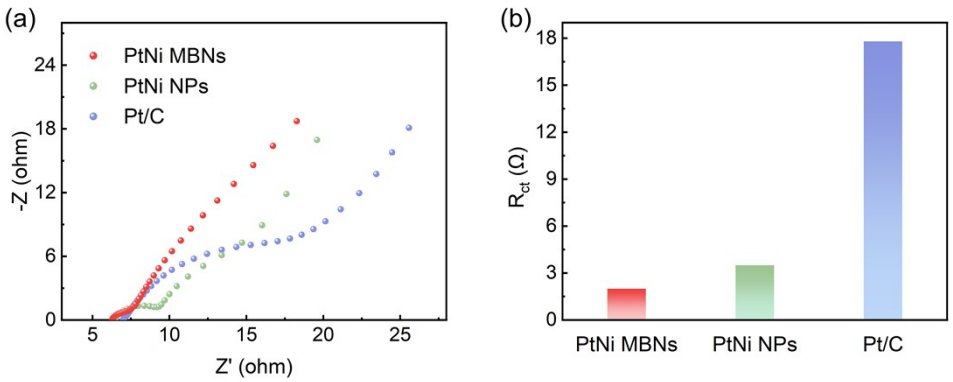

Fig. S8. (a) Nyquist plots of PtNi MBNs, PtNi NPs and and commercial Pt/C catalysts. (b) Bar chart of the R_{ct}.

Nyquist plots in Fig. S8 further corroborate the exceptional charge transfer kinetics of PtNi MBNs. The results show that the R_{ct} of PtNi MBNs (2 Ω) is the lowest compared to that of PtNi NPs (3.5 Ω) and commercial Pt/C (17.8 Ω). This lower R_{ct} value directly reflects a faster charge transfer rate, confirming that its heterogeneous interface and multi-branched structure effectively accelerate the charge transfer process. It has been demonstrated that the heterointerface and multi-branched structure of PtNi MBNs effectively accelerate charge transfer processes, providing key kinetic evidence for their exceptional HER performance.

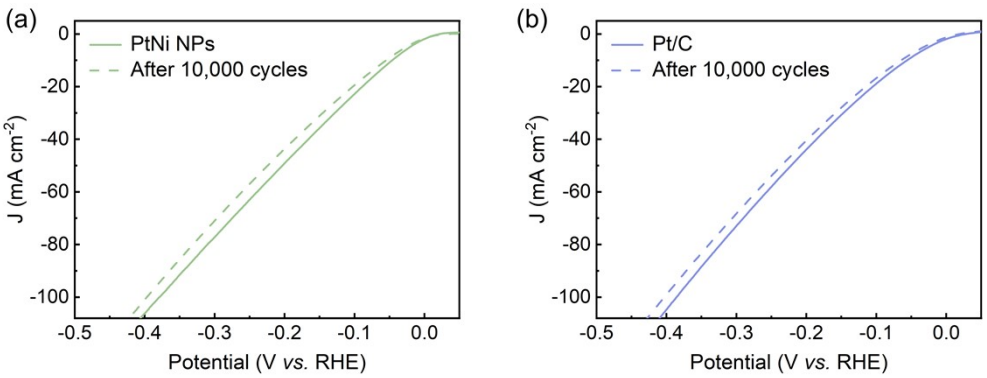

Fig. S9. LSV curves of (a) PtNi NPs and (b) commercial Pt/C before and after 10,000 CV cycles.

After 10,000 CV cycles in 1 M KOH, the overpotential of PtNi MBNs increased by only 1 mV (Fig. 4a). In contrast, both PtNi NPs and commercial Pt/C exhibited a significantly larger increase of 9 mV in Fig. S9.

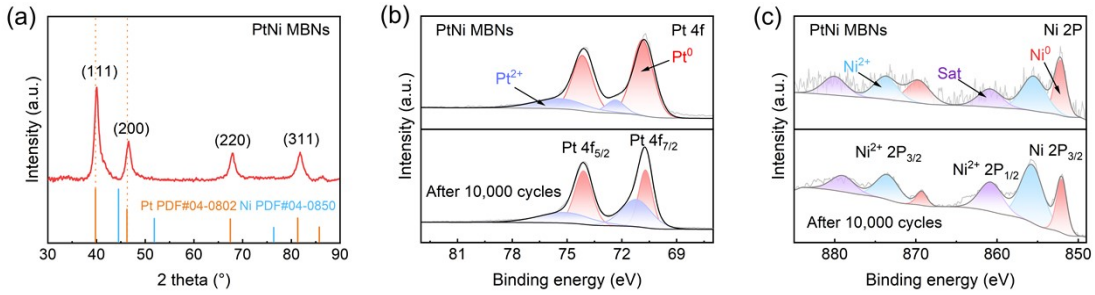

Fig. S10. (a) XRD pattern of PtNi MBNs after 10,000 CV cycles, and XPS spectra of (b) Ni 2p and (c) Pt 4f of PtNi MBNs before and after 10,000 CV cycles.

Fig. S10a presents the XRD patterns, indicating no significant shift in diffraction peaks, which verifies the preservation of the original crystal structure and composition. Furthermore, XPS spectra in Fig. S10b-c further confirmed no alteration in bulk composition post-cycling. Comparative analysis of Pt 4f and Ni 2p spectra before and after 10,000 CV cycles demonstrated well-preserved surface electronic states of the PtNi MBNs catalyst, indicating stable surface electronic structure and active sites under reaction conditions. Collectively, these characterization results demonstrate the exceptional structural and electrochemical stability of PtNi MBNs.

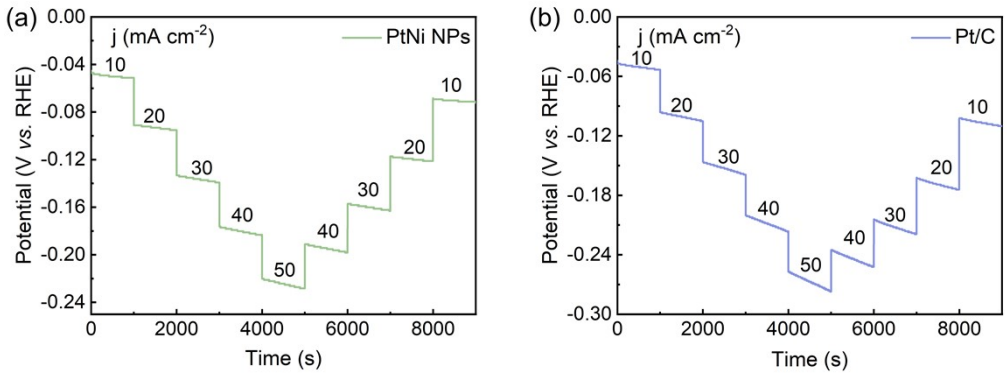

Fig. S11. Multi-step chronopotentiometry of (a) PtNi NPs and (b) commercial Pt/C under different current densities.

PtNi MBNs demonstrates exceptional current-dependent stability in multi-step chronopotentiometry measurements, maintaining consistent overpotentials while PtNi NPs and Pt/C suffer significant degradation under identical conditions (Fig. S11).

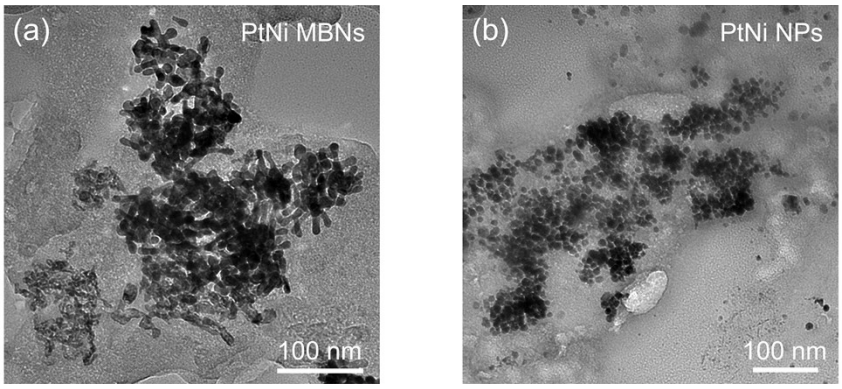

Fig. S12. TEM images of (a) PtNi MBNs and (b) PtNi NPs after chronoamperometric testing.

Fig. S12 reveals that the post-cycling TEM characterization confirms the remarkable structural stability of PtNi MBNs, as evidenced by their well-preserved branched morphology.

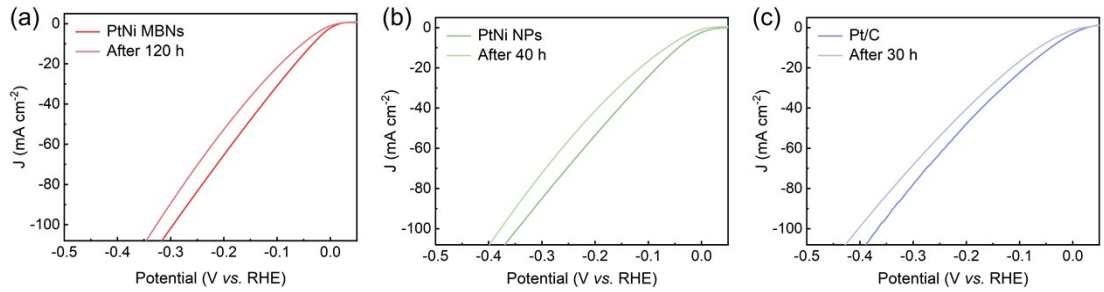

Fig. S13. LSV curves of (a) PtNi MBNs, (b) PtNi NPs and (c) commercial Pt/C before and after 120 h chronoamperometric stability testing.

As shown in Fig. S13, PtNi MBNs exhibit significantly lower performance degradation over extended testing periods. Their overpotential increase (20 mV/120 h) is substantially lower than that of PtNi NPs (22 mV/40 h) and Pt/C (23 mV/30 h), confirming that PtNi MBNs demonstrate not only morphological stability but also outstanding electrochemical stability.

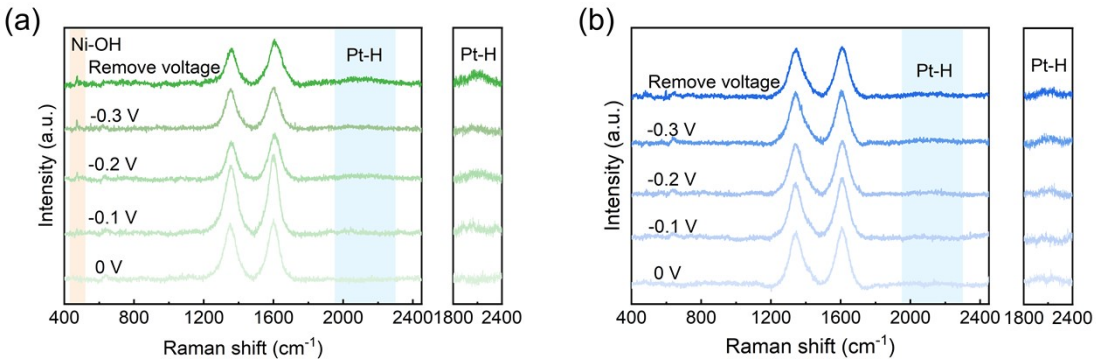

Fig. S14. *In situ* Raman spectra of PtNi MBNs (a) PtNi NPs and (b) commercial Pt/C under different applied potentials.

In situ Raman spectroscopy reveals the synergistic mechanism in PtNi MBNs, where distinct Ni–OH and Pt–H peaks appear early and remain strong during potential decrease (Fig. 4e), indicating rapid hydrogen evolution reaction kinetics. In contrast, PtNi NPs and Pt/C show delayed and much weaker peaks, with Pt/C exhibiting the weakest signal due to the lack of dual-active-site synergy, confirming the critical role of Ni–OH/Pt–H coupling in enhancing HER (Fig. S14).

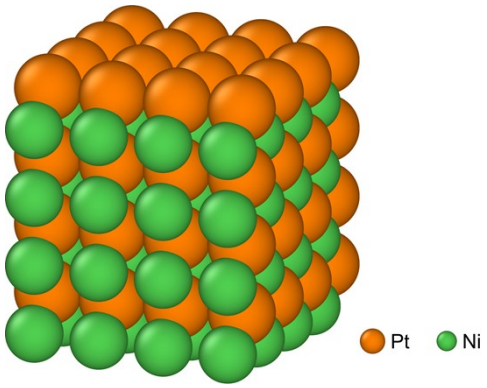

Fig. S15. Atomic model of PtNi alloy on the (001) facet.

Table S1. TEM-EDS and ICP-MS compositional analysis of PtNi MBNs.

Method	Mass ratio (wt.%)		Atomic ratio (at.%)	
	Pt	Ni	Pt	Ni
TEM-EDS	87.53	12.47	61.94	28.43
ICP-MS	27.47	7.27	62.98	29.63

Quantitative EDS analysis yielded the overall Pt:Ni atomic ratio of PtNi MBNs to be 61.94:28.43, which was close to the results from inductively coupled plasma atomic emission spectrometry.

Table S2. Comparison of overpotentials and Tafel slopes for Pt-based electrocatalysts.

Catalysts	Electrolytes	Overpotential (mV @10 mA cm^{-2})	Tafel slope (mV dec^{-1})	References
PtNi MBNs	1M KOH	9.29	29.34	This work
PVP@Pt/$Ni(OH)_2$	1M KOH	12	21.5	Ref. [8]
Pt_{SA}-Mn_3O_4	1M KOH	24	54	Ref. [9]
Pt-Ni(N) NWs	1M KOH	25	29	Ref. [10]
Pt-$Co(OH)_2$/CC	1M KOH	32	70	Ref. [11]
PtNi@Ti_3C_2 MXene	1M KOH	36	59	Ref. [12]
Pt_2Ni_3–P NWs	1M KOH	44	66	Ref. [13]
PtSA-NiSe-V	1M KOH	45	52	Ref. [14]
Pt_5/HMCS	1M KOH	46.2	48.1	Ref. [15]
Pt_{SA}-NiO	1M KOH	55	36	Ref. [16]
SANi-PtNRs	1M KOH	70	60	Ref. [17]
Pt-NiCo LDO	1M KOH	92	73	Ref. [18]

Table S3. Crystallographic information of NiPt surface model.

Parameter	Value
Space group	P1
Lattice constant a (Å)	3.8550
Lattice constant b (Å)	3.8550
Lattice constant c (Å)	3.8550
α (°)	90.0
β (°)	90.0
γ (°)	90.0
Unit cell volume ($Å^3$)	57.29

Table S4. Specific data on the adsorption times of various substances.

Adsorption	Average adsorption time
Ni-KOH	23.22
Pt-KOH	25.58
Ni-Water	9.71
Pt-Water	10.34

Table S5: Proportions of water molecule orientation configurations at different interfaces and distances

Contact Interface	Distances from Surface	O-down	Parallel	H-down
PtNi-Pt	3 Å	26.25%	48.02%	19.63%
PtNi-Ni	3 Å	30.95%	56.13%	18.99%
PtNi-Pt	5 Å	36.60%	43.99%	17.80%
PtNi-Ni	5 Å	38.45%	46.26%	16.87%

References

1 H. Berendsen, D. Spoel and R. Drunen, GROMACS: A message-passing parallel molecular dynamics implementation, *Comput. Phys. Commun.*, 1995, **91**, 43-56.

2 J. Wang, R. Wolf, J. Caldwell, P. Kollman and D. Case, Development and testing of a general amber force field, *J. Comput. Chem.*, 2004, **25**, 1157-1174.

3 A. Rappe, C. Casewit, K. Colwell, W. Goddard and W. Skiff, UFF, a full periodic table force field for molecular mechanics and molecular dynamics simulations, *J. Am. Chem. Soc.*, 1992, **114**, 10024-10035.

4 H. Lorentz, Ueber die anwendung des satzes vom virial in der kinetischen theorie der gase, *Ann. Phys.*, 1881, **248**, 127-136.

5 J. Gasteiger and M. Marsili, A new model for calculating atomic charges in molecules, *Tetrahedron Lett.*, 1978, **19**, 3181-3184.

6 A. Stukowski, Visualization and analysis of atomistic simulation data with OVITO–the open visualization tool, *Modell. Simul. Mater. Sci. Eng.*, 2010, **18**, 015012.

7 Q. Lu, A. Wang, Y. Gong, W. Hao, H. Cheng, J. Chen, B. Li, N. Yang, W. Niu, J. Wang, Y. Yu, X. Zhang, Y. Chen, Z. Fan, X. Wu, J. Chen, J. Luo, S. Li, L. Gu and H. Zhang, Crystal phase-based epitaxial growth of hybrid noble metal nanostructures on 4H/fcc Au nanowires, *Nat. Chem.*, 2018, **10**, 456-461.

8 J. Li, B. Li, H. Huang, S. Yan, C. Yuan, N. Wu, D. Guo and X. Liu, Polyvinylpyrrolidone gel based Pt/$Ni(OH)_2$ heterostructures with redistributing charges for enhanced alkaline hydrogen evolution reaction, *J. Mater. Chem. A*, 2021, **9**, 27061-27071.

9 J. Wei, K. Xiao, Y. Chen, X. Guo, B. Huang and Z. Liu, Precise anchoring of Pt single atoms in spinel Mn_3O_4 for a highly efficient hydrogen evolution reaction, *Energ. Environ. Sci.*, 2022, **15**, 4592-4600.

10 Y. Xie, J. Cai, Y. Wu, Y. Zang, X. Zheng, J. Ye, P. Cui, S. Niu, Y. Liu, J. Zhu, X. Liu, G. Wang and Y. Qian, Boosting Water Dissociation Kinetics on Pt-Ni Nanowires by N-Induced Orbital Tuning, *Adv. Mater.*, 2019, **31**, e1807780.

11 Z. Xing, C. Han, D. Wang, Q. Li and X. Yang, Ultrafine Pt nanoparticle-decorated $Co(OH)_2$ nanosheet arrays with enhanced catalytic activity toward hydrogen evolution, *ACS Catal.*, 2017, **7**, 7131-7135.

12 Y. Yan, R. Z. Zhang, Y. D. Yu, Z. M. Sun, R. C. Che, B. Wei, A. P. LaGrow, Z. C. Wang and W. Zhou, Interfacial optimization of PtNi octahedrons @Ti_3C_2 MXene with enhanced alkaline hydrogen evolution activity and stability, *Appl. Catal. B-Environ.*, 2021, **291**, 120100.

13 P. Wang, X. Zhang, J. Zhang, S. Wan, S. Guo, G. Lu, J. Yao and X. Huang, Precise tuning in platinum-nickel/ nickel sulfide interface nanowires for synergistic hydrogen evolution catalysis, *Nat. Commun.*, 2017, **8**, 14580.

14 Z. Y. Chen, X. P. Li, J. Zhao, S. Y. Zhang, J. J. Wang, H. Zhang, J. F. Zhang, Q. J. Dong, W. X. Zhang, W. B. Hu and X. P. Han, Stabilizing Pt single atoms through Pt-Se electron bridges on vacancy-enriched nickel selenide for efficient electrocatalytic hydrogen evolution, *Angew. Chem. Int. Ed.*, 2023, **62**, e08686.

15 X. K. Wan, H. B. Wu, B. Y. Guan, D. Y. Luan and X. W. Lou, Confining sub-nanometer Pt slusters in hollow mesoporous carbon spheres for boosting hydrogen evolution activity, *Adv. Mater.*, 2020, **32**, 1901349.

16 Y. M. Da, Z. l. Tian, R. Jiang, G. W. Chen, Y. Liu, Y. K. Xiao, J. F. Zhang, S. B. Xi, W. Chen, X. P. Han and W. B. Hu, Single-atom Pt doping induced p-type to n-type transition in NiO nanosheets toward self-gating modulated electrocatalytic hydrogen evolution reaction, *ACS Nano*, 2023, **17**, 18539-18547.

17 M. Li, K. Duanmu, C. Wan, T. Cheng, L. Zhang, S. Dai, W. Chen, Z. Zhao, P. Li, H. Fei, Y. Zhu, R. Yu, J. Luo, K. Zang, Z. Lin, M. Ding, J. Huang, H. Sun, J. Guo, X. Pan, W. Goddard, P. Sautet, Y. Huang and X. Duan, Single-atom tailoring of platinum nanocatalysts for high-performance multifunctional electrocatalysis, *Nat. Catal.*, 2019, **2**, 495-503.

18 Y. K. Tian, W. T. Luo, X. L. Quan, W. Y. Li, G. F. Wei, M. Bayati, Q. S. Wu, Y. Q. Fu and M. Wen, Coupling interaction between precisely located Pt single-atoms/clusters and NiCo-layered double oxide to boost hydrogen evolution reaction, *Adv. Funct. Mater.*, 2024, **34**, 05919.